Constraining the Progenitor System of the Type Ia Supernova 2021aefx

Griffin Hosseinzadeh[1] , David J. Sand[1] , Peter Lundqvist[2] , Jennifer E. Andrews[3] , K. Azalee Bostroem[4,15] , Yize Dong (董一泽)[5] , Daryl Janzen[6] , Jacob E. Jencson[1] , Michael Lundquist[7] , Nicolas E. Meza Retamal[5] , Jeniveve Pearson[1] , Stefano Valenti[5] , Samuel Wyatt[1] , Jamison Burke[8,9] , D. Andrew Howell[8,9] , Curtis McCully[8,9] , Megan Newsome[8,9] , Estefania Padilla Gonzalez[8,9] , Craig Pellegrino[8,9] , Giacomo Terreran[8,9] , Lindsey A. Kwok[10] , Saurabh W. Jha[10] , Jay Strader[11] , Esha Kundu[11] , Stuart D. Ryder[12,13] , Joshua Haislip[14] , Vladimir Kouprianov[14] , and Daniel E. Reichart[14]

[1] Steward Observatory, University of Arizona, 933 North Cherry Avenue, Tucson, AZ 85721-0065, USA; griffin0@arizona.edu
[2] Oskar Klein Centre, Department of Astronomy, Stockholm University, Albanova University Centre, SE-106 91 Stockholm, Sweden
[3] Gemini Observatory, 670 North A'ohoku Place, Hilo, HI 96720-2700, USA
[4] Department of Astronomy, University of Washington, 3910 15th Avenue NE, Seattle, WA 98195-0002, USA
[5] Department of Physics and Astronomy, University of California, Davis, 1 Shields Avenue, Davis, CA 95616-5270, USA
[6] Department of Physics & Engineering Physics, University of Saskatchewan, 116 Science Place, Saskatoon, SK S7N 5E2, Canada
[7] W. M. Keck Observatory, 65-1120 Māmalahoa Highway, Kamuela, HI 96743-8431, USA
[8] Las Cumbres Observatory, 6740 Cortona Drive, Suite 102, Goleta, CA 93117-5575, USA
[9] Department of Physics, University of California, Santa Barbara, CA 93106-9530, USA
[10] Department of Physics and Astronomy, Rutgers, the State University of New Jersey, 136 Frelinghuysen Road, Piscataway, NJ 08854-8019, USA
[11] Center for Data Intensive and Time Domain Astronomy, Department of Physics and Astronomy, Michigan State University, East Lansing, MI 48824, USA
[12] School of Mathematical and Physical Sciences, Macquarie University, NSW 2109, Australia
[13] Astronomy, Astrophysics and Astrophotonics Research Centre, Macquarie University, Sydney, NSW 2109, Australia
[14] Department of Physics and Astronomy, University of North Carolina, 120 East Cameron Avenue, Chapel Hill, NC 27599, USA
Received 2022 May 4; revised 2022 June 9; accepted 2022 June 27; published 2022 July 15

Abstract

We present high-cadence optical and ultraviolet light curves of the normal Type Ia supernova (SN) 2021aefx, which shows an early bump during the first two days of observation. This bump may be a signature of interaction between the exploding white dwarf and a nondegenerate binary companion, or it may be intrinsic to the white dwarf explosion mechanism. In the case of the former, the short duration of the bump implies a relatively compact main-sequence companion star, although this conclusion is viewing-angle dependent. Our best-fit companion-shocking and double-detonation models both overpredict the UV luminosity during the bump, and existing nickel-shell models do not match the strength and timescale of the bump. We also present nebular spectra of SN 2021aefx, which do not show the hydrogen or helium emission expected from a nondegenerate companion, as well as a radio nondetection that rules out all symbiotic progenitor systems and most accretion disk winds. Our analysis places strong but conflicting constraints on the progenitor of SN 2021aefx; no current model can explain all of our observations.

Unified Astronomy Thesaurus concepts: Binary stars (154); Supernovae (1668); Type Ia supernovae (1728); White dwarf stars (1799)

Supporting material: data behind figures

1. Introduction

The explosions of carbon-oxygen white dwarfs (WDs) as Type Ia supernovae (SNe Ia) have long been important tools in astrophysics, their use as standardizable candles having led to the discovery of dark energy (Riess et al. 1998; Perlmutter et al. 1999). However, despite decades of intense study, SN Ia progenitor systems and explosion mechanisms are still not fully understood (see reviews by Howell 2011; Maoz et al. 2014; Maguire 2017, and Jha et al. 2019). The progenitor WD must be in a binary (or higher) system in order to accrete material and ignite, but the companion star may either be a main-sequence or giant star (the single-degenerate scenario; Whelan & Iben 1973) or another WD (the double-degenerate scenario;

Iben & Tutukov 1984; Webbink 1984). Additionally, the explosion may be a pure deflagration (Nomoto et al. 1984), a deflagration that transitions to a detonation after the WD is unbound (a delayed detonation; Khokhlov 1991), a detonation triggered by an earlier helium-shell detonation (a double detonation; Nomoto 1982; Livne 1990; Woosley & Kasen 2011), or another more extreme model (e.g., a dynamical or violent merger; Benz et al. 1989; Lorén-Aguilar et al. 2009; Katz & Dong 2012; Kushnir et al. 2013). See Hoeflich (2017) for a review of explosion mechanisms.

The very early light curves of SNe Ia are among the best probes of the progenitor system and explosion physics. Whereas most of their evolution is uniform (such that they can be used for cosmology), their light curves during the first few days after explosion can reveal important clues about their progenitor systems and explosion triggers. For example, Kasen (2010) predicted that, given a favorable viewing angle, the collision between the SN ejecta and a nondegenerate companion star would result in an observable UV excess over a smooth rise, an effect that would disappear after only a few

---

days (when most SNe are discovered). However, such a "bump" might also be explained by an unusual distribution of radioactive ^{56}Ni in the SN ejecta (e.g., Magee & Maguire 2020), or it might be an expected feature of a sub-Chandrasekhar-mass explosion (e.g., Polin et al. 2019).

Over the past decade, only a handful of nearby SNe Ia have been discovered early enough to test these hypotheses. SN 2011fe followed a smooth $L \propto t^2$ rise, from which Nugent et al. (2011) and Bloom et al. (2012) derived a stellar radius that confirmed a WD progenitor. Li et al. (2011) and Nugent et al. (2011) also rule out a nondegenerate companion to SN 2011fe at high significance. Cao et al. (2015) showed an initial decline in the UV light curve of the peculiar (02es-like) SN Ia iPTF14atg, and Marion et al. (2016) showed a slight excess in the early U and B light curves of the normal Type Ia SN 2012cg compared to a power-law rise, both of which were interpreted as interaction with a nondegenerate companion (though see Shappee et al. 2018 for the latter event). Hosseinzadeh et al. (2017) presented a time-resolved excess in the early U, B, and g light curves of SN 2017cbv, with a ~6 hr cadence over the first 5 days, which could be explained by a nondegenerate companion. However, the companion-shocking model greatly overpredicted the strength of the bump in the UV bands. Jiang et al. (2017) concluded that the early, red flash in MUSSES1604D arose from a helium-shell detonation. Miller et al. (2018) presented a ~2 mag rise over the first day of the g-band light curve of iPTF16abc, which they interpreted as the effect of circumstellar interaction and/or nickel mixing. Dimitriadis et al. (2019) and Shappee et al. (2019) both presented a two-component power-law rise in the high-cadence Kepler 2 light curve of SN 2018oh (Li et al. 2019), but they disagree about its origin with respect to the companion-shocking, nickel-mixing, and double-detonation models. Miller et al. (2020), Burke et al. (2021), and Tucker et al. (2021) showed that the extremely luminous UV excess during the first ~5 days of the 02es-like SN 2019yvq also could not be fully explained by any single model, although Siebert et al. (2020) conclude it was a double detonation. Jiang et al. (2021) concluded that the <1 day flash in SN 2020hvf was due to circumstellar interaction. Ni et al. (2022) presented a unique red bump in the early light curve of SN 2018aoz, which they interpreted as an overdensity of iron-peak elements in the outer layers of the ejecta. Most recently, Deckers et al. (2022) found six new events with early excesses in the g and/or r band in a sample of 115 SNe Ia, and J. Burke et al. (2022, in preparation) will present a uniform analysis of 9 nearby well-observed SNe Ia.

An additional probe of the nature of the binary companion comes from nebular spectroscopy. In the case of a nondegenerate companion, the SN ejecta should be enriched with hydrogen and/or helium stripped from the companion, which should appear in emission once the ejecta are mostly transparent (Marietta et al. 2000; Pan et al. 2010, 2012; Liu et al. 2012, 2013; Botyánszki et al. 2018; Dessart et al. 2020). Lundqvist et al. (2013, 2015) note that forbidden oxygen and calcium lines may also arise from interaction with a nondegenerate companion, but these lines are weak and difficult to disentangle from the underlying SN emission.

Hydrogen emission has been detected in the so-called SNe Ia-CSM, which are thought to have symbiotic nova progenitors (e.g., Dilday et al. 2012), but these are only a rare subclass of SNe Ia ($\lesssim 5\%$; Dubay et al. 2022). Narrow emission lines have not been detected in the vast majority of normal SNe Ia (e.g., Maguire et al. 2016; Sand et al. 2019; Tucker et al.

2020 for recent compilations), even where the light curve showed an early bump (e.g., Sand et al. 2018; Dimitriadis et al. 2019; Tucker et al. 2019). This appears to disfavor the single-degenerate scenario for most normal SNe Ia. However, three recent detections of Hα in fast-declining SNe Ia suggest that this channel may be physically allowed for some subluminous SNe Ia (Kollmeier et al. 2019; Vallely et al. 2019; Prieto et al. 2020; Elias-Rosa et al. 2021).

Here we present the case of the normal Type Ia SN 2021aefx, which was discovered within hours of explosion by the Distance Less Than 40 Mpc (DLT40) survey (Tartaglia et al. 2018). The early unfiltered light curve from DLT40, with an average cadence of ≈ 2 hr over the first 5 days, shows a subtle excess with respect to a power-law rise during the first two days of observation. In addition, its daily-cadence UV light curve shows an initial decrease over the first two observations. We refer to these and similar excesses in the U, B, and g bands as the "bump" throughout our analysis. After describing the observations of SN 2021aefx in Section 2, we compare the light curve to models of companion shocking, sub-Chandrasekhar-mass WD explosions, and explosions of WDs with surface nickel in Section 3, in an attempt to explain the cause of the early bump. In Section 4, we describe the unique first spectrum of SN 2021aefx, and in Section 5 we search for hydrogen and helium emission in its nebular spectra. In Section 6 we present constraints from the nondetection of SN 2021aefx in the radio. We discuss the implications of this analysis for its progenitor system and explosion mechanism in Section 7.

2. Observations and Data Reduction

SN 2021aefx was discovered by DLT40 on 2021-11-11.343 UT at an unfiltered brightness of 17.25 ± 0.05 mag and was not detected on 2021-11-06.328 UT to an unfiltered limit of 19.35 mag (Valenti et al. 2021). Its J2000 coordinates are $\alpha = 04^{\rm h}19^{\rm m}53{\overset{\rm s}{.}}400$ and $\delta = -54°56'53{\overset{''}{.}}09$ according to Gaia Photometric Science Alerts,[16] $1{\overset{'}{.}}2$ (6.2 kpc) southeast of the center of its intermediate spiral host, NGC 1566 (de Vaucouleurs et al. 1995). It was initially classified as a Type I (hydrogen-poor) SN by Bostroem et al. (2021) based on a unique early spectrum (see Section 4 for more details). Its Type Ia classification was secured the next day by Onori et al. (2021).

2.1. UV/Optical Data

We immediately initiated a high-cadence photometric follow-up campaign using the 1 m and 0.4 m telescope networks of Las Cumbres Observatory (Brown et al. 2013) and the Ultraviolet/Optical Telescope (UVOT; Roming et al. 2005) on the Neil Gehrels Swift Observatory (Gehrels et al. 2004). We measured aperture photometry on the Las Cumbres images using `lcogtsnpipe` (Valenti et al. 2016) and calibrated to images of the RU149 standard field (Rubin et al. 1974) taken on the same night with the same telescope. RU149 catalogs are from Stetson (2000) for UBV (Vega magnitudes) and the SDSS Collaboration et al. (2017) for gri (AB magnitudes). We measured photometry on the UVOT images using the High-Energy Astrophysics Software (HEA-Soft; NASA HEASARC 2014) in a $3''$ aperture centered at the position of SN 2021aefx. We used a set of 10 UVOT pre-

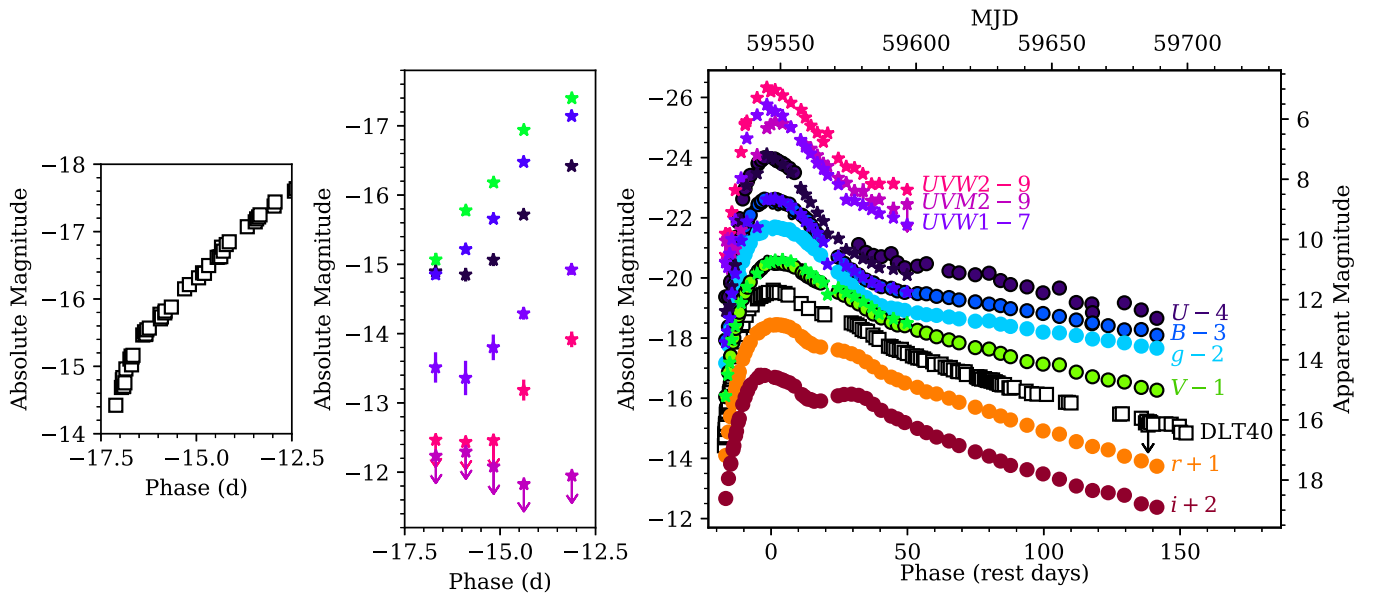---

[16] https://www.wis-tns.org/object/2021aefx

Figure 1. Light curve of SN 2021aefx from Las Cumbres Observatory (circles), DLT40 (squares), and Swift (stars), offset and binned by 0.01 days for clarity. Phase is given with respect to maximum light in the B band, estimated in Section 3. The left panel highlights the very high-cadence unfiltered light curve from DLT40, with no offset, showing a bump lasting $\sim$2 days. The middle panel highlights the early Swift photometry, with no offsets, showing an initial decrease in the U and $UVW1$ filters.

(The data used to create this figure are available.)

explosion archival observations taken between 2020 June 12 and 2020 October 21 to subtract the background contamination by emission from the host galaxy in the same aperture. We applied the zero-points of Breeveld et al. (2011) with the time-dependent sensitivity corrections updated in 2020. We correct for Milky Way extinction of $E(B-V) = 0.0079$ mag (Schlafly & Finkbeiner 2011) and host-galaxy extinction of $E(B-V) = 0.097$ mag (see Section 2.3), according to the Fitzpatrick (1999) extinction law, and a Tully & Fisher (1977) distance of 18.0 ± 2.0 Mpc ($\mu = 31.28 \pm 0.23$ mag; Sabbi et al. 2018). The resulting light curve of SN 2021aefx is shown in Figure 1.

We also obtained optical spectroscopy of SN 2021aefx using the FLOYDS spectrograph on Las Cumbres Observatory's 2 m Faulkes Telescope South (FTS; Brown et al. 2013), the High Resolution Spectrograph (HRS) and the Robert Stobie Spectrograph (RSS) on the South African Large Telescope (SALT; Buckley et al. 2006), and the Goodman High-Throughput Spectrograph on the Southern Astrophysical Research Telescope (SOAR; Clemens et al. 2004). We reduced these spectra using the FLOYDS pipeline (Valenti et al. 2014), the SALT HRS MIDAS pipeline (Kniazev et al. 2016, 2017), PySALT (Crawford et al. 2010), the Goodman pipeline (Torres et al. 2017), and/or other standard PyRAF routines (Science Software Branch at STScI 2012). We also include the public classification spectrum of Onori et al. (2021) from the ESO Faint Object Spectrograph and Camera 2 (EFOSC2) on the New Technology Telescope (NTT; Buzzoni et al. 1984). The spectral series is logged in Table 1 and plotted in Figure 2, corrected for the redshift of the host galaxy ($z = 0.005017$; Allison et al. 2014).

2.2. Radio Data

SN 2021aefx was observed in the radio with the Australia Telescope Compact Array (ATCA) on two occasions (Kundu et al. 2021): 2021 November 13 between UT 14:30 and 17:30,

and 2021 November 19 from UT 13:00 to 17:00. For the first epoch, the central frequencies were 5.5 GHz, 9 GHz, and 18 GHz, using a bandwidth of 2 GHz, while for the second epoch only the central frequencies 5.5 GHz and 9 GHz were used. The observation and reduction procedures follow Lundqvist et al. (2020). PKS B1934−638 was used as the primary calibrator, and the quasar J0441−5154 was used as the secondary calibrator.

As reported by Kundu et al. (2021), no radio emission was detected down to 3σ upper limits of 70 μJy beam^{-1} at 5.5 GHz, 60 μJy beam^{-1} at 9.0 GHz, and 50 μJy beam^{-1} at 18 GHz for the first epoch, and 40 μJy beam^{-1} at 5.5 GHz and 30 μJy beam^{-1} at 9.0 GHz for the second. The total on-source time at each frequency was 1.0 hr during the first epoch and 3.0 hr during the second. For a host-galaxy distance of 18.0 Mpc, this implies upper limits on the luminosity at the first epoch of $2.71\,(2.33)\,(1.94) \times 10^{25}$ erg s^{-1} Hz^{-1} for 5.5 (9) (18) GHz and $1.55\,(1.16) \times 10^{25}$ erg s^{-1} Hz^{-1} for 5.5 (9) GHz at the second.

2.3. Host-galaxy Extinction

Our high-resolution ($R \approx 40{,}000$) SALT spectrum, taken 16.4 days after peak, shows strong DNa I in absorption at the redshift of the host galaxy (Figure 3, top). We measure an equivalent width of $W_\lambda = 0.077$ nm, which corresponds to a host-galaxy extinction of $E(B-V) = 0.097$ mag, according to the relationship of Poznanski et al. (2012) with the recalibration of Schlafly et al. (2010).

We also estimate the host-galaxy extinction by comparing it to the Lira (1996) Law, following the procedure of Phillips et al. (1999). We fit a straight line with a fixed slope of -0.0118 mag day^{-1} to the $B-V$ color curve of SN 2021aefx between 30 and 60 days after V-band maximum, corrected for Milky Way extinction only, using weighted least-squares fitting (Figure 3, bottom). This line is offset from the Lira Law by

Table 1
Log of Spectroscopic Observations

MJD	Telescope	Instrument	Phase
59529.859	SALT	RSS	−16.6[a]
59530.868	SALT	RSS	−15.6
59531.118	SOAR	Goodman	−15.3
59531.266	NTT	EFOSC	−15.2
59531.703	FTS	FLOYDS	−14.8
59532.073	SALT	RSS	−14.4
59532.838	SALT	RSS	−13.6
59533.625	FTS	FLOYDS	−12.9
59533.856	SALT	RSS	−12.6
59534.498	FTS	FLOYDS	−12.0
59535.073	SALT	RSS	−11.4
59536.445	FTS	FLOYDS	−10.0
59536.855	SALT	RSS	−9.6
59538.070	SALT	RSS	−8.4
59538.853	SALT	RSS	−7.6
59550.598	FTS	FLOYDS	+4.0
59556.805	SALT	RSS	+10.2
59558.477	FTS	FLOYDS	+11.9
59559.087	SOAR	Goodman	+12.5
59560.992	SALT	RSS	+14.4
59561.478	FTS	FLOYDS	+14.9
59563.000	SALT	HRS	+16.4
59564.498	FTS	FLOYDS	+17.9
59567.672	FTS	FLOYDS	+21.0
59568.010	SALT	RSS	+21.4
59569.067	SOAR	Goodman	+22.4
59572.542	FTS	FLOYDS	+25.9
59577.480	FTS	FLOYDS	+30.8
59582.540	FTS	FLOYDS	+35.8
59589.594	FTS	FLOYDS	+42.8
59591.919	SALT	HRS	+45.2
59594.590	FTS	FLOYDS	+47.8
59597.890	SALT	HRS	+51.1
59615.419	FTS	FLOYDS	+68.5
59630.480	FTS	FLOYDS	+83.5
59634.105	SOAR	Goodman	+87.1
59648.447	FTS	FLOYDS	+101.4
59665.060	SOAR	Goodman	+117.9
59668.398	FTS	FLOYDS	+121.2
59681.390	FTS	FLOYDS	+134.2

Note.
[a] The spectrum presented here is a rereduction of the data published by Bostroem et al. (2021) on the Transient Name Server.

$E(B − V)_{\rm host} = 0.044$ mag. Given that our two estimates agree to within the scatter in the Lira Law (∼0.05 mag; Phillips et al. 1999), we adopt the former estimate, $E(B − V)_{\rm host} = 0.097$ mag, throughout the remainder of our analysis.

3. Light Curves and Color Curves

The most striking feature of our early photometry is the ∼2 day bump in the extremely high-cadence DLT40 unfiltered light curve (FWHM = 357–871 nm; Figure 1, left). As the bump subsides, we also observe a decline in the bluest detected bands (U and UVW1; Figure 1, center) and a rapid reddening in the $U − B$, $B − V$, and $g − r$ color curves (Figure 4). Compared to SNe 2017cbv (Hosseinzadeh et al. 2017) and 2018oh (Dimitriadis et al. 2019; Li et al. 2019; Shappee et al. 2019), which also had well-sampled early bumps, the bump in SN 2021aefx lasts about half as long (2 days versus 5 days). In

the following sections, we fit three classes of models to our photometry to explore the cause of the early bump.

Apart from the bump, the light curve of SN 2021aefx is quite typical for an SN Ia. We fit a fourth-order polynomial to the B-band light curve of SN 2021aefx around maximum light (∼5 days before to ∼20 days after), using only data from Las Cumbres Observatory's 1 m telescopes for consistency. The polynomial gives a peak of $M_B = −19.63 \pm 0.02$ mag at MJD 59546.54. We adopt this as phase = 0 throughout our figures and tables. The light curve declines by $\Delta m_{15}(B) = 0.90 \pm 0.02$ mag over the 15 days after that peak. This is consistent with the slow and luminous end of the Phillips (1993) relation, which gives confidence in the distance we adopt above, despite its large uncertainty. We note in passing that the SALT2 (Guy et al. 2007) and MLCS2k2 (Jha et al. 2007) SN Ia templates also provide good fits to the optical (BgVri) light curves of SN 2021aefx around maximum light.

3.1. Companion-shocking Model

Kasen (2010) predicts that this type of early light-curve bump can arise when the SN ejecta collide with a nondegenerate binary companion, which shock-heats the ejecta and causes them to briefly become bluer and more luminous. We fit the light curve of SN 2021aefx with a model composed of a SiFTO SN Ia template (Conley et al. 2008) and a companion-shocking component from Kasen (2010), following the procedure of Hosseinzadeh et al. (2017) now released as part of the Light Curve Fitting package (Hosseinzadeh & Gomez 2020). While the effect of companion shocking depends on the viewing angle, here we employ the formulae for the "isotropic equivalent luminosity," which is approximately the strength of the effect for viewing angles less than 30°–40° from the binary axis (Kasen 2010). In performing this fit, we exclude data from Las Cumbres Observatory's 0.4 m telescopes, which have greater scatter, and we assume that the unfiltered DLT40 light curve can be approximately fit by the r-band SiFTO template. (We confirmed that the early DLT40 and r-band light curves are in good agreement.) Unlike Hosseinzadeh et al. (2017), we do not require additional multiplicative factors on the r and i SiFTO templates, nor on the U shock component, to achieve a reasonable fit. Instead, we fit for small time shifts in the U and i SiFTO templates to improve the match during the light-curve rise (after the bump). We also include an intrinsic scatter term σ, such that the effective uncertainty on each point is increased by a factor of $\sqrt{1 + \sigma^2}$. This allows for scatter not accounted for by the model, as well as photometric uncertainties that are potentially underestimated, in order to estimate more realistic uncertainties on the model parameters. The model parameters and their respective priors and best-fit values are listed in Table 2. The light curve and best-fit model are displayed in Figure 5 (left).

The best-fit binary separation is $a = 1.8\,R_\odot$. If we assume the companion is in Roche lobe overflow ($\frac{a}{R} \approx 2$–3; Eggleton 1983; Kasen 2010), this implies a companion radius of $R \approx 0.7\,R_\odot$. This and the other values are degenerate with the viewing angle, which we do not account for here (see above), but nonetheless, the order of magnitude suggests a low-mass main-sequence star. The best-fit explosion time ($t_0 = 59529.19^{+0.07}_{−0.12}$) indicates that our discovery image was taken 3.5 rest-frame hours after explosion. The remaining parameters are "nuisance" parameters for our analysis, but we note that the artificial time shifts we applied to certain bands of the SiFTO
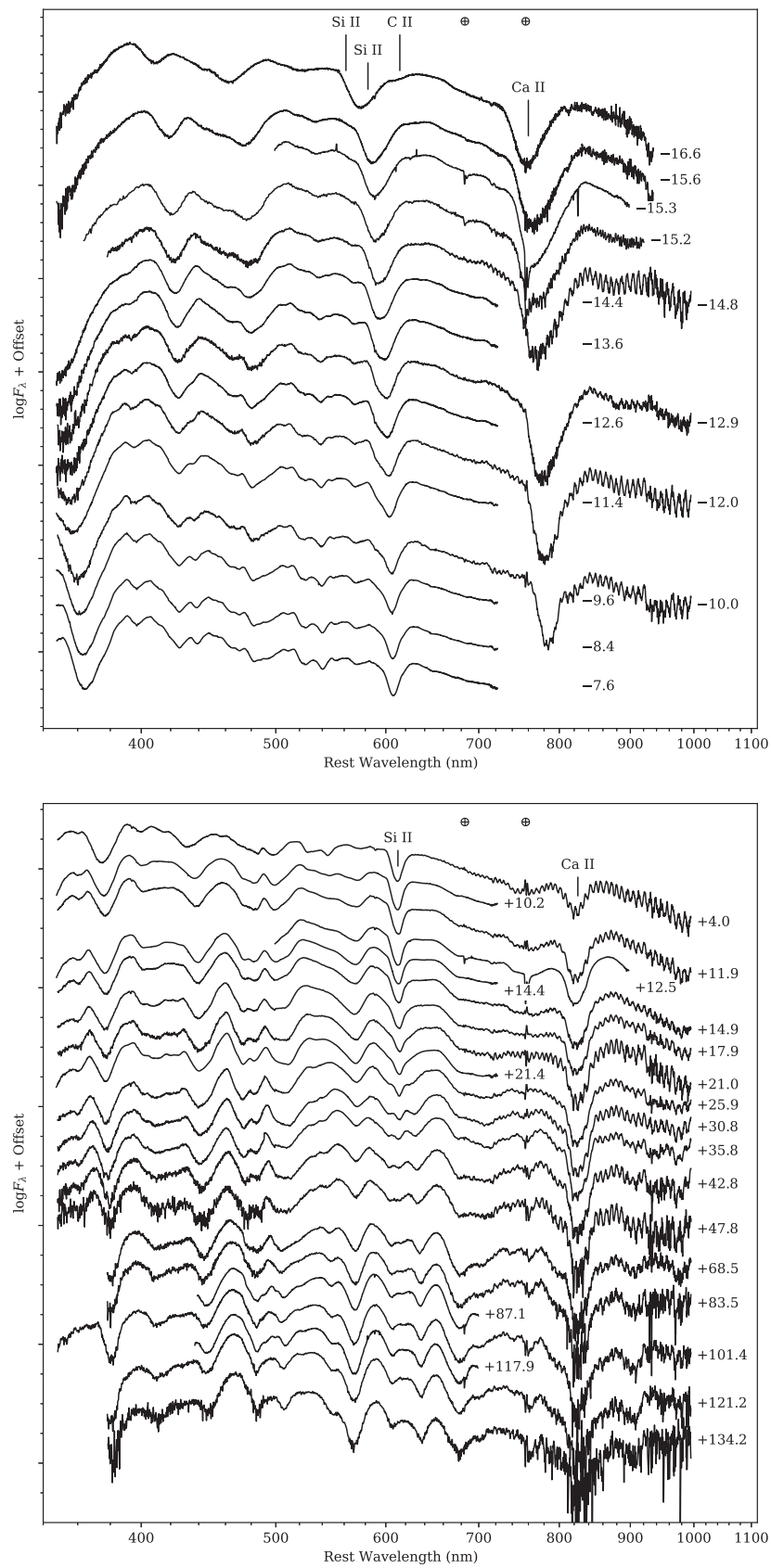
Figure 2. Low-resolution spectra of SN 2021aefx. Phases are marked to the right of each spectrum in rest-frame days after the *B*-band peak. The strongest absorption features in the first spectrum are marked. See Figure 6 for a more detailed view. Telluric wavelengths are marked with the ⊕ symbol.

(The data used to create this figure are available.)

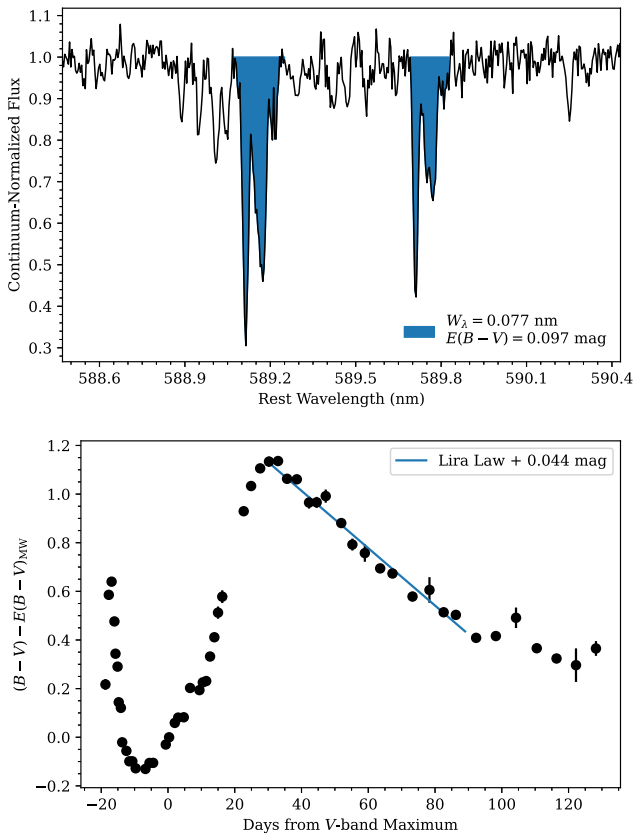**Figure 3.** Top: high-resolution spectrum of SN 2021aefx in the region around DNa I. We measure an equivalent width of $W_\lambda = 0.077$ nm, corresponding to a host-galaxy extinction of $E(B-V)_{\rm host} = 0.097$ mag. Bottom: Milky Way extinction-corrected $B-V$ color curve of SN 2021aefx. A linear fit to the color on the radioactively powered tail shows an offset of $E(B-V)_{\rm host} = 0.044$ mag with respect to the Lira Law. These are both consistent to within the scatter in the Lira Law, so we adopt the former estimate: $E(B-V)_{\rm host} = 0.097$ mag.

model are small (<1 day) and that the stretch is close to 1, confirming again that this is a typical SN Ia.

As in SN 2017cbv (Hosseinzadeh et al. 2017), which showed a similar early bump, the best-fit model drastically overpredicts the UV luminosity (Figure 5, bottom right). The shock component alone is 10, >28, and >18 times stronger than the observed luminosity in the *UVW1*, *UVM2*, and *UVW2* bands, respectively. However, unlike in SN 2017cbv, our high-cadence early Swift light curve shows an initial decline in *UVW1*. In other words, there is a significant UV bump, but it is not as strong as the model predicts.

3.2. Sub-Chandrasekhar-mass Models

Polin et al. (2019) also predict similar early bumps for explosions of sub-Chandrasekhar-mass WDs arising from the double-detonation mechanism. For each of the 39 models in their grid, we apply time shifts between 0 and 3 days, in half-day increments, between their explosion time and our explosion time estimate from Section 3.1. We then calculate the reduced χ^2 ($\bar\chi^2$) statistic for each shifted model compared to our *UBgVri* light curve from the Las Cumbres Observatory 1 m telescopes. Several models have a reasonable fit around peak, the best being a 1.1 $M_\odot$ WD with a 0.01 $M_\odot$ helium shell ($\bar\chi^2 = 1083$; number of observations $n = 52$), but this model has no early bump at all, underpredicting our first epoch of observations by several magnitudes.

To search for models with a good fit to the bump specifically, we repeat this procedure with the $U-B$ color curve. The best-fit model in this case ($\bar\chi^2 = 579$; $n = 22$) is shown in Figure 5 (right) with a time shift of 0.5 days. This model is an edge-lit double detonation of a 0.9 $M_\odot$ WD with a 0.08 $M_\odot$ helium shell. The morphology of the bump is a good fit, with very blue but rapidly reddening colors for ∼2 days. However, as in the companion-shocking model, this sub-Chandrasekhar-mass model severely overpredicts the bump in the U band. At the same time, it does not reach the relatively bright peak magnitude that we observe in any band, and the colors are much redder than observed after maximum light.

3.3. Nickel-shell Models

We also compared the light curves and color curves of SN 2021aefx to the models of Magee et al. (2020), in which they explode WDs with radioactive ^{56}Ni mixed into the outer layers using the TURTLS radiative transfer code (Magee et al. 2018). We repeat the time shift and $\bar\chi^2$ calculation as in Section 3.2. Again we are able to find good fits around peak. However, none of these provide a good fit to the early bump. In many cases, this is because the models only begin >2 days after explosion. However, as noted by Magee et al. (2020), most models in their grid do not show an early bump at all.

A more promising set of nickel models come from Magee & Maguire (2020), who set out to reproduce the early bumps in SNe 2017cbv and 2018oh. These models include a shell of nickel artificially placed into the outer ejecta. The model set is smaller and tailored to two specific SNe, but nonetheless we repeat the time shift and $\bar\chi^2$ calculation, this time using both $U-B$ and $B-V$ colors. We find that the SN 2017cbv model with a shell of 0.02 $M_\odot$ of ^{56}Ni centered on a mass coordinate of 1.35 $M_\odot$ with a width of 0.18 $M_\odot$ provides a reasonable fit to both the light curves ($\bar\chi^2 = 205$; $n = 187$) and color curves ($\bar\chi^2 = 211$; $n = 34$) of SN 2021aefx, with no time shift. Although this model provides a better fit to the light-curve peak than the double-detonation model, the early bump is not strong enough to match our first epoch of observations. Further modeling tailored to SN 2021aefx could potentially provide a better fit. However, Magee & Maguire (2020) also note that their models greatly overpredict the strength of the UV bump. We discuss all the above models further in Section 7.

3.4. Circumstellar Interaction

Piro & Morozova (2016) explore the possibility that early excesses in SNe Ia arise from nickel mixing into the outer layers plus a small amount of circumstellar material (CSM). We repeated our fitting process for these models and found some reasonable fits to the $U-B$ and $B-V$ color curves: all the models with 0.3 $M_\odot$ of CSM and mixing widths of 0.05 $M_\odot$ (Figure 13 of Piro & Morozova 2016) have $\bar\chi^2 \approx 500$ ($n = 22$). However, these models are very poor fits to the light curve; the bumps are much more extreme than we observe. In general, the bumps in these models are not blue enough, in the sense that it is not possible to produce a strong enough bump in the U band without producing almost equal-strength bumps in the redder bands. (Note that their figures show V-band bumps, whereas the bump in SN 2021aefx is almost invisible in V).
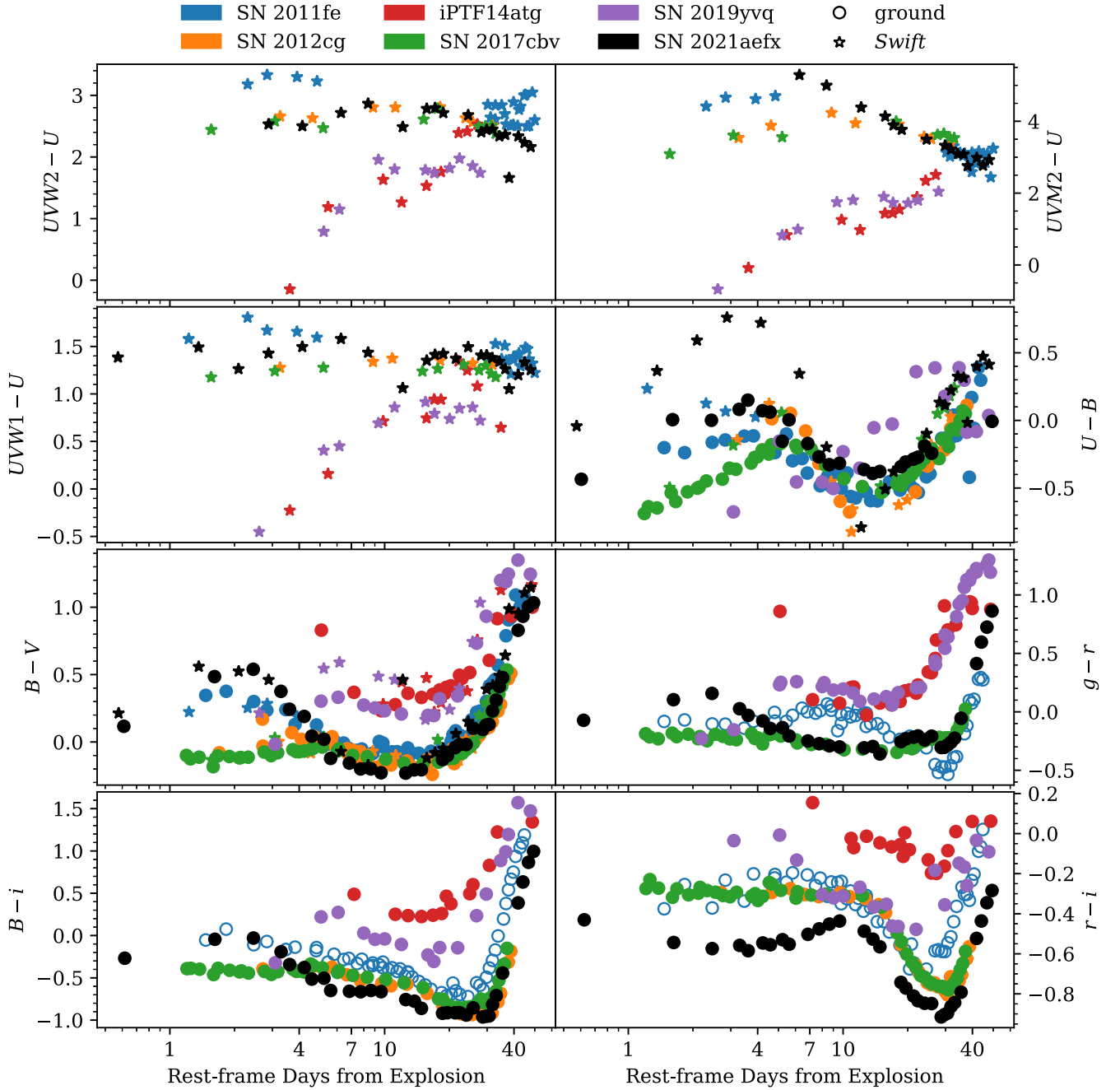
Figure 4. Extinction-corrected color curves of SN 2021aefx compared to SN 2011fe (Zhang et al. 2016) and other SNe Ia with early excesses: SN 2012cg (Marion et al. 2016), iPTF14atg (Cao et al. 2016), SN 2017cbv (Hosseinzadeh et al. 2017), and SN 2019yvq (Burke et al. 2021). For the purposes of the logarithmic time axis, we adopt explosion estimates from the aforementioned authors and use $MJD_0 = 59529.19$ (Section 3.1) for SN 2021aefx. The early color behavior of SN 2021aefx is similar to SN 2017cbv, but the abrupt change in slope (in $U - B$ and other colors) happens earlier (at ~2 days instead of ~5 days). In the companion-shocking interpretation, this implies a tighter binary and thus a more compact companion (Kasen 2010).

3.5. Doppler Shift

Ashall et al. (2022) recently proposed that some UV bumps can be explained simply by shifting common SN Ia spectral features into and out of the observed filter passbands. In particular, they claim that the u-band bump in SN 2021aefx is caused by the Ca II H&K absorption feature shifting to wavelengths lower than the peak sensitivity of the u filter, due to the very high expansion velocities in its earliest spectrum (a preliminary reduction of the same data we present here). However, this mechanism can only explain bumps in filters where there is a strong spectral slope across the

passband. Ashall et al. (2022) suggest that $UVM2$ is another such band, due to the strong absorption from iron-peak elements around 200–250 nm, but they do not discuss the Swift photometry of SN 2021aefx specifically, which shows the bump in $UVW1$.

Importantly, this mechanism cannot explain the bump in our early unfiltered light curve. Whereas shifting the Ca II H&K feature to shorter wavelengths can significantly increase the u/U-band flux, it barely affects the unfiltered optical light curve, even though the CCD has some sensitivity in the UV, as it is averaged over a much broader wavelength range. As a demonstration, we follow the procedure of Ashall et al.

Table 2
Model Parameters

Parameter	Variable	Prior Shape	Prior Parameters[a]		Best-fit Value[b]	Units
			Companion-shocking Model (Kasen 2010)			
Explosion time	t_0	Uniform	59526.34	59529.34	$59529.19^{+0.07}_{-0.12}$	MJD
Binary separation	a	Uniform	0	1	$0.012^{+0.004}_{-0.003}$	10^{13} cm
Ejecta mass $\times$ velocity^7	Mv^7	Log-uniform	0.1	500	90^{+120}_{-50}	M_{Ch} $(10^4$ km s$^{-1})^7$
			SiFTO Model (Conley et al. 2008)			
Time of B maximum	t_{max}	Uniform	59542.09	59548.09	59546.54 ± 0.03	MJD
Stretch	s	Log-uniform	0.5	2	1.010 ± 0.002	dimensionless
Time shift in U	Δt_U	Gaussian	0	1	$+0.71^{+0.08}_{-0.07}$	d
Time shift in i	Δt_i	Gaussian	0	1	$+0.52 \pm 0.10$	d
			Combined Model			
Intrinsic scatter	σ	Half-Gaussian	0	1	12.9 ± 0.4	dimensionless

Notes.
[a] The "Prior Parameters" column lists the minimum and maximum for a uniform distribution, and the mean and standard deviation for a Gaussian distribution.
[b] The "Best-fit Value" column is determined from the 16th, 50th, and 84th percentiles of the posterior distribution, i.e., median $\pm 1\sigma$.

(2022) to calculate synthetic photometry[17] from our early spectrum both as observed and redshifted[18] by 16,000 km s^{-1}. We find that the spectrum as observed is 0.55 mag brighter in U and <0.01 mag brighter in the DLT40 band than the lower-velocity version. In other words, the bump in the unfiltered light curve must also include contributions from the redder bands.

As an additional precaution, we repeated our fit of the companion-shocking model from Section 3.1 without the U-band light curve. (The Swift photometry was already not included.) Our best-fit model is nearly identical to the one shown in Figure 5 (left), including the value of the binary separation. This confirms that, even if the U-band photometry is "contaminated" by the Ca II H&K Doppler effect, the optical light curves alone lead to the same conclusions.

4. Early Spectra

The initial spectrum of SN 2021aefx shows an unusually deep and broad absorption feature around 570 nm in the rest frame of the host galaxy. We show a detail of this feature compared to our other premaximum spectra in Figure 6. If we attribute this line to Si II at 635.5 nm, we infer a very high expansion velocity of $\sim$29,500 km s^{-1}. However, the non-Gaussian shape of the line, even at later phases, may indicate the presence of two velocity components, as well as blending with another Si II line at 597.2 nm. We also observe a second absorption component on the red side of this feature, which we attribute to C II 658.0 nm. Only $\sim$10%–30% of SNe Ia show carbon in their early optical spectra (Parrent et al. 2011; Folatelli et al. 2012; Silverman & Filippenko 2012; Wyatt et al. 2021), and this feature in SN 2021aefx is one of the strongest observed to date. Unburned carbon has been interpreted as a signature of asymmetry or clumpiness in the WD explosion

(Höflich & Stein 2002; Röpke et al. 2007; Shen & Bildsten 2014), which serves as a probe of the explosion mechanism. For example, unburned carbon is not expected for Chandrasekhar-mass delayed-detonation models (Kasen et al. 2009) or from sub-Chandrasekhar-mass double-detonation models (Fink et al. 2010; Polin et al. 2019). Several other SNe Ia with early light-curve excesses have exhibited strong, early carbon signatures, including iPTF16abc (Miller et al. 2018), SN 2017cbv (Hosseinzadeh et al. 2017), and SN 2018oh (Li et al. 2019), a suggestive feature that we will explore in future work.

Our spectrum near maximum light (+4 days) closely resembles near-maximum spectra of several normal SNe Ia, particularly SN 1981B, which spectroscopic classifiers Gelato (Harutyunyan et al. 2008), SNID (Blondin & Tonry 2007), and Superfit (Howell et al. 2005) all place in the top three best matches. In this spectrum, where the lines are not blended, we fit a linear continuum minus a Gaussian to the Si II lines at 635.5 nm and 597.2 nm. We measure equivalent widths of 10.6 ± 0.7 nm and 1.7 ± 0.6 nm, respectively, both at a velocity of $11\,390 \pm 30$ km s^{-1}. This places it near the boundary of the "core normal" and "broad line" subclasses of Branch et al. (2006) and in the high-velocity subclass of Wang et al. (2013). Along with the light-curve widths in Section 3 ($\Delta m_{15}(B) = 0.90$ mag) and Section 3.1 ($s = 1.010$), these measurements indicate that SN 2021aefx is a typical SN Ia that could be used for cosmology. More detailed modeling of the unique early spectrum, along with a full spectroscopic analysis, will be presented by L. A. Kwok et al. (2022, in preparation).

5. Nebular Spectroscopy

We measure complementary constraints on the progenitor system of SN 2021aefx using the late-time SOAR spectrum (117.9 days after B-band maximum), which was taken with the Goodman Spectrograph's red camera, 600 line mm^{-1} grating, and a 1″ slit, resulting in an $R \approx 1250$. If the progenitor system of SN 2021aefx had a nondegenerate companion star, as the early light curve hints at, then models predict that the SN ejecta will ablate the companion and lead to narrow hydrogen or helium emission lines (FWHM ≈ 1000 km s^{-1}) $\gtrsim$100 days

---

[17] Rather than extrapolate the spectrum into the UV and infrared to cover the DLT40 bandpass, we only integrate over wavelengths covered by our spectrum. This is equivalent to assuming that the transmission-weighted average F_ν is the same outside our wavelength coverage as it is inside.

[18] We do this to compare with their results, although we agree with their caveat that simply redshifting a spectrum is not the correct way to simulate lower-velocity lines.
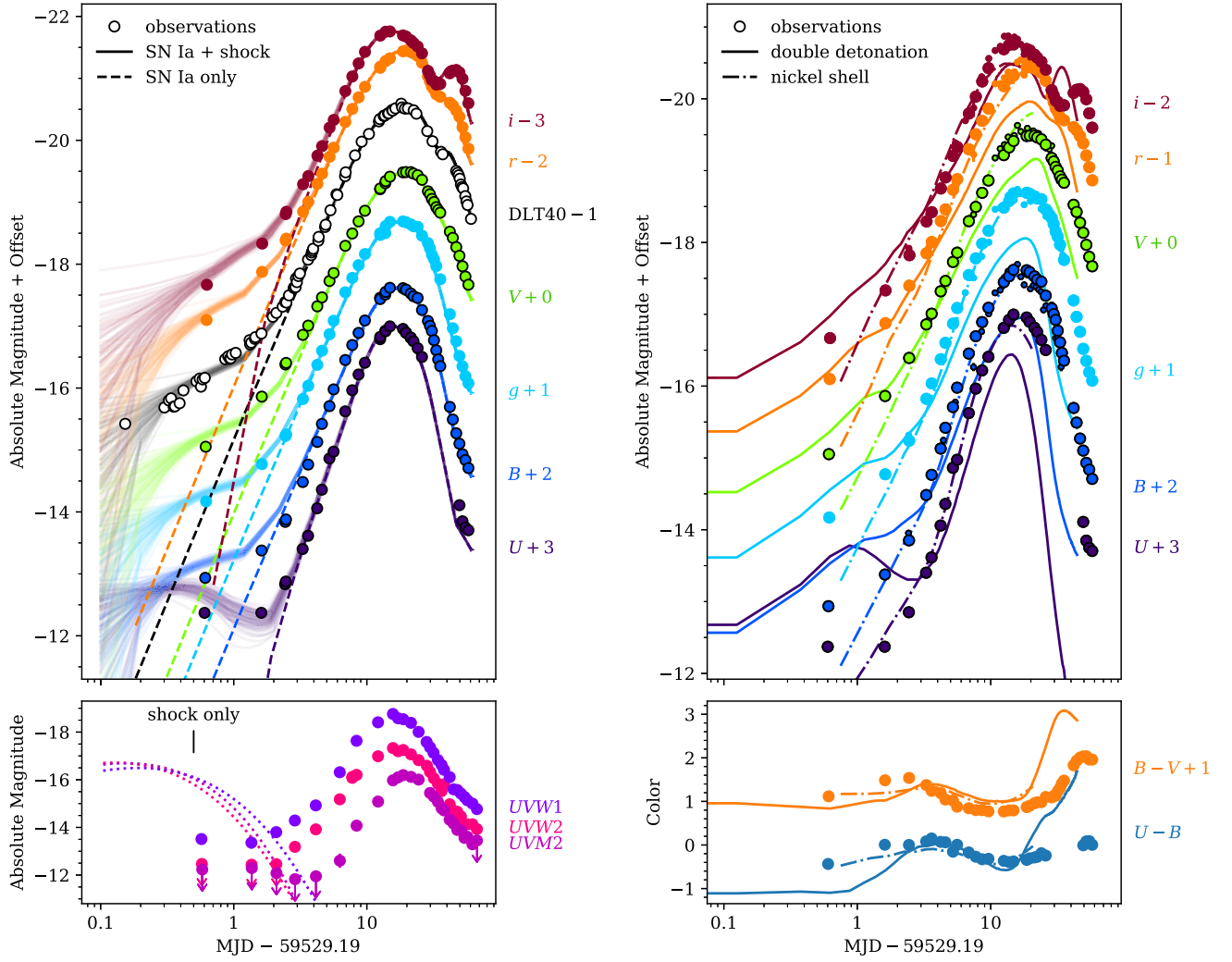
Figure 5. Left: fitting the companion-shocking model of Kasen (2010) to the light curve of SN 2021aefx. The solid lines in the top panel show the best-fit SiFTO +Kasen model, with the SiFTO model alone shown with dashed lines. The model reproduces the early optical light curve quite well, but the shock component alone (SiFTO does not extend into the UV) significantly overestimates the early UV flux (bottom). Right: best-fit edge-lit double-detonation model from Polin et al. (2019, solid lines) and nickel-shell model from Magee & Maguire (2020, dotted–dashed lines) compared to the observed light curve (top) and $U - B$ and $B - V$ color curves (bottom) of SN 2021aefx. This double-detonation model is the explosion of a 0.9 $M_\odot$ WD with a 0.08 $M_\odot$ helium shell. The model reproduces the early color well but overestimates the absolute magnitude of the bump, while also failing to reproduce the peak absolute magnitude and postpeak colors. The nickel-shell model is a fiducial model of SN 2017cbv plus a shell of 0.02 $M_\odot$ of ^{56}Ni centered on a mass coordinate of 1.35 $M_\odot$ with a width of 0.18 $M_\odot$. This model reproduces the peak better but does not show a strong enough bump in the light curves or color curves.

after the explosion (e.g., most recently Botyánszki et al. 2018; Dessart et al. 2020). The models predict $\gtrsim$0.1 $M_\odot$ of stripped hydrogen, although there is diversity in the expected strength and shape of the resulting emission line, which will depend on the details of the explosion, nondegenerate companion, and radiation transfer physics employed.

Direct inspection of the SOAR spectrum reveals no hydrogen or helium emission features, and we set quantitative limits on any narrow Hα or He I (either λ5875 Å and λ6678 Å) emission using the methodology of Sand et al. (2018, 2019). Briefly, we take the flux-calibrated and extinction-corrected spectrum and bin to the native resolution. Following this, we smoothed the spectrum on scales larger than the expected emission (FWHM $\approx$ 1000 km s^{-1}) using a second-order Savitzky & Golay (1964) filter with a width of 130 Å. Any hydrogen or helium feature with a width similar to that expected in the single-degenerate scenario would be apparent in the difference between the unsmoothed and smoothed versions of the spectrum.

To set quantitative limits on our Hα and He I nondetections, we directly implant emission lines into our data, assuming a line width of 1000 km s^{-1} and a peak flux that is three times the root mean square of the residual spectrum described above. This results in flux and luminosity (assuming D=18.0 Mpc) limits for (i) Hα of 1.6×10^{-15} erg s^{-1} cm^{-2} and 6.3×10^{37} erg s^{-1}; (ii) He I λ5875 Å of 4.8×10^{-15} erg s^{-1} cm^{-2} and 1.9×10^{38} erg s^{-1}; and (iii) He I λ6678 Å of 1.6×10^{-15} erg s^{-1} cm^{-2} and 6.3×10^{37} erg s^{-1}, respectively. These limits are also listed in Table 3. This Hα luminosity limit is comparable to, or fainter than, the recent detections identified in three fast-declining SNe Ia (Kollmeier et al. 2019; Prieto et al. 2020; Elias-Rosa et al. 2021).

To translate these hydrogen and helium luminosity limits to masses, we utilize the radiation transport model sets of Botyánszki et al. (2018) and Dessart et al. (2020) and refer the reader directly to those works for details. In brief, the 3D radiation transport results of Botyánszki et al. (2018) presented simulated SN Ia spectra at 200 days after explosion, based on
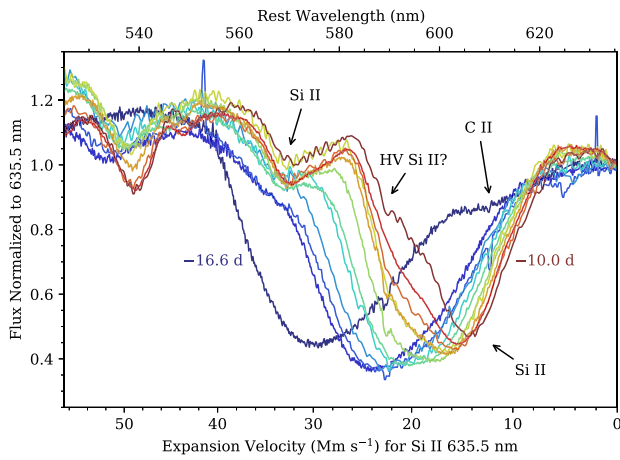
Figure 6. Line identification in the premaximum spectra of SN 2021aefx. Colors are a nonlinear function of time; exact phases are listed in Table 1. Our initial spectrum (−16.6 days, dark purple) is dominated by a very broad absorption feature around 570 nm (in the rest frame of the host galaxy). By comparison to later spectra (e.g., at −10 days, dark red), this line likely consists of Si II 597.2 nm, Si II 635.5 nm, and C II 658.0 nm. There may also be a high-velocity (HV) component of Si II 635.5 nm that makes the absorption profile flatter than a Gaussian. The presence of unburned carbon in the early spectrum disfavors the sub-Chandrasekhar-mass double-detonation model for SN 2021aefx.

Table 3
Summary of Results

Parameter	Value
Last nondetection	MJD 59524.328
First detection	MJD 59529.343
Distance	18.0 ± 2.0 Mpc
Distance modulus	31.28 ± 0.23 mag
Redshift	0.005017
Milky Way $E(B-V)$	0.0079 mag
Host-galaxy $E(B-V)$	0.097 mag
Peak absolute magnitude (B)	-19.63 ± 0.02 mag
Peak time (B)	MJD 59546.54
$\Delta m_{15}(B)$	0.90 ± 0.02 mag
Si II velocity (−17 d)	$\approx 29\,500$ km s^{-1}
Si II velocity (+4 d)	$11\,390 \pm 30$ km s^{-1}
Si II 635.5 nm EW (+4 d)	10.6 ± 0.7 nm
Si II 597.5 nm EW (+4 d)	1.7 ± 0.6 nm
Hα luminosity	$< 6.3 \times 10^{37}$ erg s^{-1}
He I $\lambda 5875$ Å luminosity	$< 1.9 \times 10^{38}$ erg s^{-1}
He I $\lambda 6678$ Å luminosity	$< 6.3 \times 10^{37}$ erg s^{-1}
Stripped H mass (Botyánszki)	$\lesssim 4.5 \times 10^{-4} M_\odot$
Stripped H mass (Dessart)	$\lesssim (5–6) \times 10^{-4} M_\odot$
Stripped He mass (Botyánszki)	$\lesssim (2–5) \times 10^{-3} M_\odot$

the SN Ia ejecta–companion interaction simulations of Boehner et al. (2017). The simulated spectra show $L_{H\alpha} \approx (4.5–15.7) \times 10^{39}$ erg s^{-1} for their main-sequence, subgiant, and red-giant companion star models (corresponding to $M_{strip} \sim 0.2$–$0.4\,M_\odot$), roughly two orders of magnitude brighter than our detection limit. To quantify our stripped mass limit, we adopt the quadratic fitting relation between Hα (and He I $\lambda 5875$ Å and $\lambda 6678$ Å) luminosity and stripped hydrogen/helium mass (Equation (1) in Botyánszki et al. 2018, updated by Sand et al. 2018) and make a correction for the epoch of our observations (117.9 days after B-band max, or 135.2 days after explosion), similar to that done in Botyánszki et al. (2018).

This leads to a stripped hydrogen mass limit of $M_{H,strip} \lesssim 4.5 \times 10^{-4}\,M_\odot$, and a helium mass limit of $M_{He,strip} \lesssim 5.4 \times 10^{-3}\,M_\odot$ and $M_{He,strip} \lesssim 2.4 \times 10^{-3}\,M_\odot$ for the He I $\lambda 5875$ Å and $\lambda 6678$ Å lines, respectively.

We also constrain the amount of stripped hydrogen based on 1D radiative transfer calculations from several different delayed-detonation models (DDC0, DDC15, and DDC25; Blondin et al. 2013), including non-LTE physics and optical depth effects, as presented by Dessart et al. (2020). Here we take the available model grids, which run from 100 to 300 days after explosion and interpolate them to the explosion epoch of SN 2021aefx. With these models, our stripped hydrogen mass limit is between $M_{H,strip} \lesssim (5–6) \times 10^{-4}\,M_\odot$, depending on the model used. These same radiative transfer simulations produce weak or ambiguous helium emission lines (aside from the He I $\lambda 10830$ Å line, which is unavailable to us), so we do not calculate stripped helium mass limits for this model framework. We tabulate our hydrogen and helium luminosity and stripped mass limits in Table 3.

We recommend the collection of a sequence of nebular spectra to further constrain and search for signatures of the single-degenerate scenario out to later times. Other works have suggested searching for other narrow emission lines, such as [O I]$\lambda 6300$ Å and Ca II $\lambda\lambda 7291,7324$ Å, which may be sensitive to helium star companions in particular (e.g., Lundqvist et al. 2013). While our deep SOAR spectrum constrains the luminosity of the [O I]$\lambda 6300$ Å line to be $L_{[O\,I]} < 6.3 \times 10^{37}$ erg s^{-1}, data at later times will further constrain the progenitor system of SN 2021aefx.

6. Radio Nondetection

We model the radio emission from the SN in the same way as Lundqvist et al. (2020). That is, the emission arises as a result of circumstellar interaction when electrons are accelerated to relativistic speeds behind the supernova blast wave where significant magnetic fields are also generated. The relativistic electrons radiate synchrotron emission. For a power-law distribution of the electron energies, $dN/dE = N_0 E^{-p}$, where $E = \gamma m_e c^2$ is the energy of the electrons and γ is the Lorentz factor, the intensity of optically thin synchrotron emission $\propto \nu^{-\alpha}$, where $\alpha = (p-1)/2$. We have used $p = 3$, as this has been shown to be a good choice for SNe Ibc (Chevalier & Fransson 2006).

The structure of the CSM depends on the progenitor system. For a double-degenerate progenitor system, one may expect a constant-density medium (see below), whereas for most single-degenerate systems, some sort of wind mass loss is likely to occur. We probe the latter by assuming a constant mass-loss rate, $\dot{M}$, and a constant wind speed, v_w. For this scenario, the density of the CSM decreases with distance from the progenitor system as $\rho(r) = \dot{M}/(4\pi r^2 v_w)$.

For the SN ejecta, we employ a model called N100 (Röpke et al. 2012; Seitenzahl et al. 2013) to test the single-degenerate scenario, as was also used by Lundqvist et al. (2020). This is a delayed-detonation model where the ignition occurs in 100 sparks in the central region. The total mass and asymptotic kinetic energy of the ejecta for N100 are $1.4\,M_\odot$ and 1.45×10^{51} erg, respectively. The density profile of the ejecta in N100 is only given for velocities $\leqslant 2.8 \times 10^4$ km s^{-1}. For faster ejecta, a power-law density structure, $\rho_{ej} \propto r^{-n}$, was added. As in the models of Lundqvist et al. (2020), who modeled radio upper limits for several nearby SNe Ia, we have
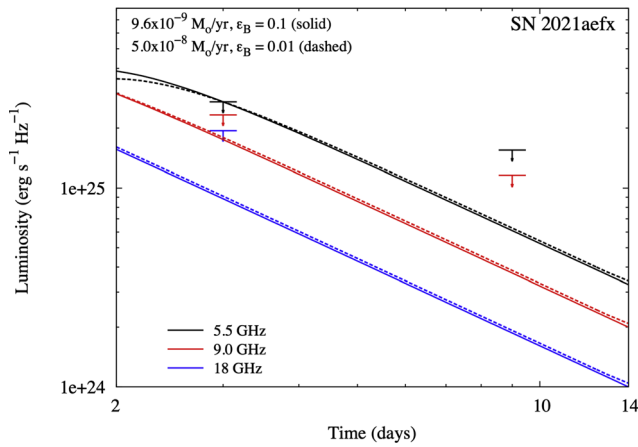
Figure 7. Radio data for SN 2021aefx (Kundu et al. 2021) compared to models at various frequencies for a $\rho(r) \propto r^{-2}$ wind. Models use $\dot{M} = 0.96\ (5.0)\ \times\ 10^{-8} M_\odot\ \mathrm{yr}^{-1}\ (v_w/100\ \mathrm{km\ s}^{-1})$ for $\epsilon_B = 0.1\ (0.01)$, with solid lines being for $\epsilon_B = 0.1$. Common parameters in both models are $\epsilon_e = 0.1$, $T_\mathrm{bright} = 5 \times 10^{10}$ K, $n = 13$ and $v_w = 100\ \mathrm{km\ s}^{-1}$. The most constraining observation is at 5.5 GHz on day 3.

assumed $n = 13$ (see Kundu et al. 2017 for a discussion on n). The same value for n facilitates comparison with those nearby supernovae. For the same reason, we have also assumed the same value for the brightness temperature of the radio emission at the frequency at which the optical depth of synchrotron self-absorption is unity as in Lundqvist et al. (2020), namely $T_\mathrm{bright} = 5 \times 10^{10}$ K (see Björnsson & Lundqvist 2014 for further discussion on T_bright).

In Figure 7 we show the predicted radio emission from our model. Using the best-fit explosion time from Section 3.1, the two epochs of radio observations occurred 3 and 9 days after explosion. The ratio of $\dot{M}/v_w$ has been tuned to give the highest luminosity possible that does not conflict with observational limits. Solid lines are for high efficacy of conversion of shock energy to magnetic field energy density in the postshock region behind the supernova blast wave. If we define $\epsilon_B = u_B/u_\mathrm{th}$, where u_th is the postshock thermal energy density and u_B is the magnetic field energy density, $\epsilon_B = 0.1$ in this model. Dashed lines are for $\epsilon_B = 0.01$. (In both models we have used $\epsilon_\mathrm{rel} = 0.1$, where $\epsilon_\mathrm{rel} = u_\mathrm{rel}/u_\mathrm{th}$, and u_rel is the energy density in relativistic electrons.) As can be seen, a higher wind density is needed to compensate for less efficient conversion to magnetic field energy density. For $\epsilon_B = 0.1\ (0.01)$ the wind density is described by $\dot{M} = 0.96\ (5.0)\ \times\ 10^{-8} M_\odot\ \mathrm{yr}^{-1}\ (v_w/100\ \mathrm{km\ s}^{-1})$. For both choices of ϵ_B, the constraining observation is that at 5.5 GHz 3 days after the explosion. The light curves only differ significantly at $t \lesssim 3$ days in the 5.5 GHz band. Here, synchrotron self-absorption plays a role in the $\epsilon_B = 0.01$ model.

From the compilation of nearby SNe Ia by Lundqvist et al. (2020), we note that only one SN Ia has been younger at the time of the first radio observation, namely SN 2011fe (see Chomiuk et al. 2016). Figure 7 shows that early observations are essential to constrain any wind material. The compilation of Lundqvist et al. (2020) further shows that SN 2021aefx is one of the most constraining cases in that sense, only clearly surpassed by SNe 2011fe, 2012cg, and 2014J. Despite this, it is difficult to rule out the majority of formation channels of single-degenerate scenarios, even if ϵ_B were as high as ~0.1 (see Lundqvist et al. 2020). As discussed by Lundqvist et al. (2020), we may expect ϵ_B in the range of 0.01–0.1 for young

supernovae, but there is considerable uncertainty (Reynolds et al. 2021).

In the companion-shocking model, radio emission is likely to be produced as a result of the interaction between the SN and the binary companion. However, at the time of the first radio observations, the blast wave had already reached $2.3\ (1.8) \times 10^{15}$ cm for the $\epsilon_B = 0.1\ (0.01)$ models. This means that the companion interaction occurred deep inside the ejecta. For example, the outermost ejecta with power-law slope $n = 13$ stretch between 2.5×10^{14} and 2.3×10^{15} cm on day 3. Assuming that this shell mainly consists of carbon, the electron density at its innermost radius is ~3.9×10^8 cm^{-3}, if carbon is singly ionized. If we further assume a temperature of 10^4 K, the free–free optical depth through this shell alone is ~1.1×10^4 at 5.5 GHz. Free–free opacity through ejecta at velocities $\lesssim 2.8 \times 10^4$ km s^{-1} will add to this optical depth. It is therefore safe to state that no radio emission could have escaped from the companion interaction region on day 3 unless we could view this through a hole in the ejecta.

For the sub-Chandrasekhar model in Section 3.2, the time between explosion and first radio observation is closer to 4 days. Even if the N100 model may not be ideal for this case, Figure 7 shows that a higher value for $\dot{M}/v_w$ can be accommodated if the time between the explosion and the first radio observation is increased. If we use N100 and 4 days after explosion, $\dot{M} = 1.23\ (6.4)\ \times\ 10^{-8} M_\odot\ \mathrm{yr}^{-1}\ (v_w/100\ \mathrm{km\ s}^{-1})$ for $\epsilon_B = 0.1\ (0.01)$, respectively.

For a situation with a constant-density ambient medium, which may be the case for a double-degenerate scenario, the expected radio flux increases with time (e.g., Kundu et al. 2017; Lundqvist et al. 2020). To test this, we invoke the violent merger model of Pakmor et al. (2012), simulating the merger of two C/O degenerate stars with masses of $1.1\ M_\odot$ and $0.9\ M_\odot$. The total mass and asymptotic kinetic energy of the ejecta for this model are $1.95\ M_\odot$ and 1.7×10^{51} erg, respectively. If we use 5.5 GHz from our second data set and assume that the data probe interaction between the supernova and the ambient medium 10 days after explosion, the upper limit on the density of the ambient medium is 200 (1180) cm^{-3} for $\epsilon_B = 0.1\ (0.01)$.

In summary, the radio data cannot probe any possible direct interaction between the ejecta and a binary companion, but they can be used to put a limit on the density of the ambient medium outside ~2×10^{15} cm. In a single-degenerate scenario, the mass-loss rate of the progenitor system is $\gtrsim 1 \times 10^{-8} M_\odot\ \mathrm{yr}^{-1}\ (v_w/100\ \mathrm{km\ s}^{-1})$ for $\epsilon_B = 0.1$. For the double-degenerate scenario, or the single-degenerate scenario with spun-up/spun-down super-Chandrasekhar-mass WDs (Di Stefano et al. 2011; Justham 2011), where mass transfer no longer occurs at the time of explosion, a near-uniform density of the ambient medium is expected. However, the radio data are not ideal to test this, because the likely density is of order 1 cm^{-3}, and our upper limit on the density is 200 cm^{-3} for $\epsilon_B = 0.1$. The limits on mass-loss rates and ambient medium density are a factor of ~5 higher for $\epsilon_B = 0.01$.

7. Progenitor Constraints

Taken together, our constraints from the optical/UV light curves (Section 3), nebular spectra (Section 5), and radio observations (Section 6) place strong but conflicting constraints on the nature of the progenitor of SN 2021aefx. The nondetections of stripped material and circumstellar interaction decisively favor the double-degenerate scenario. On the other

hand, the most recent numerical models of double-degenerate explosion mechanisms, even those with unusual nickel distributions, do not match our observed light curves.

Intriguingly, there are good matches to the bump among the color curves of the sub-Chandrasekhar SNe Ia modeled by Polin et al. (2019). However, several pieces of evidence work against this progenitor model for SN 2021aefx. (1) The luminosity and Si II velocity of SN 2021aefx at maximum light place it in Polin et al.'s class of Chandrasekhar-mass WD explosions.[19] (2) Polin et al. (2019) predict that thick helium shells (like our best-fit model; $0.08\,M_\odot$ of helium) would produce nearly featureless spectra during the bump (see their Figure 8), whereas our spectrum has very strong, broad absorption features (Figure 6). (3) Polin et al. (2019) predict that the spectra at peak would be heavily line blanketed in the blue, which we do not observe (Figure 2). (4) Unburned carbon is not expected in double detonations (Polin et al. 2019), yet C II absorption is clearly detected in our premaximum spectra.[20] (5) Polin et al. (2021) predict that sub-Chandrasekhar SNe Ia will show strong [Ca II] emission in their nebular spectra, which we do not observe, at least up to 134 days after maximum light (Figure 2). As such, although the bump color roughly matches our observations, we do not favor the double-detonation mechanism for SN 2021aefx.

The companion-shocking model of Kasen (2010) appears to show a much better fit to the light curve, except for the fact that it greatly overpredicts the UV luminosity of the bump. This is most likely a weakness of the assumption of a blackbody SED for the shock component. While the shock front itself may radiate as a blackbody, much of this light will be reprocessed by the SN ejecta before reaching the observer, imprinting an SN Ia spectrum, which shows strong absorption lines in the UV, on the shock component as well. (Hosseinzadeh et al. 2017 applied a suppression factor to the U-band shock component in SN 2017cbv for this reason.) Modeling the shock emission from SN ejecta colliding with a binary companion using a more realistic SED is a promising avenue for future theoretical work.

When comparing the light curves around maximum light, it is important to remember the very different provenances of these SN Ia models: The models of Polin et al. (2019) are physical, whereas the SiFTO model of Conley et al. (2008) is purely observational. In addition, our fitting procedure for the latter, which scales each band independently and applies time offsets to the two bands where they are necessary, essentially guarantees a good fit to the luminosity and colors at peak. Therefore, our claim of a good fit is not based on the peak of the light curve, but rather on the fact that it is possible for the companion-shocking model to produce a bump with roughly the right shape and timescale in all the optical bands.

Our limits on stripped hydrogen are ∼2–3 orders of magnitude below expectations from recent radiative transfer models for nebular emission in the single-degenerate scenario (Botyánszki et al. 2018; Dessart et al. 2020), which generically predict stripped hydrogen in the range $M_{\rm H,strip} \approx 0.1$–$0.5\,M_\odot$. There are important caveats to these results, as they depend on the physics and limited parameter space explored by the simulations we compare our observations to. Future work

including SNe Ia with a variety of explosion strengths, companion separations, and companion types would greatly enhance this probe for progenitor studies. To our knowledge, SN 2021aefx is the third normal SN Ia with an early light-curve excess that did not show hydrogen/helium emission-line features in their late-time spectra, after SN 2017cbv (Sand et al. 2018) and SN 2018oh (Dimitriadis et al. 2019; Tucker et al. 2019). Nebular spectra of the subluminous SN 2019yvq, which also had an early excess, did not show hydrogen/helium emission either (Siebert et al. 2020; Burke et al. 2021; Tucker et al. 2021).

Our radio limits rule out ejecta–wind interaction for mass-loss rates of order $10^{-8}\,M_\odot\,{\rm yr}^{-1}$ or higher (assuming $v_w \approx 100$ km s^{-1}), which excludes all symbiotic systems (e.g., Seaquist et al. 1993). This is in agreement with Chomiuk et al. (2016), who showed that ≲10% of SNe Ia come from symbiotic progenitors. They also rule out the majority of single-degenerate systems with high accretion rates, which are expected to give rise to optically-thick disk winds (e.g., Badenes et al. 2007). Though not able to rule out all possible CSM configurations, our limits are among the strongest pieces of evidence of a clean circumbinary environment around the exploding WD, nearly on par with the deep X-ray nondetections of SNe 2017cbv and 2020nlb (Sand et al. 2021).

8. Summary and Conclusions

We have presented high-cadence optical and UV photometry of the normal Type Ia SN 2021aefx showing a UV excess during the first ∼2 days of observation. This bump can either be explained as a collision between the ejecta and a main-sequence binary companion or as an intrinsic property of a sub-Chandrasekhar-mass explosion. Both of our best-fit models broadly reproduce the light-curve morphology but with specific weaknesses that must be addressed before reaching a strong conclusion. We also presented nebular spectroscopy of SN 2021aefx showing no evidence of hydrogen- or helium-rich material stripped from a nondegenerate binary companion, as well as radio observations showing no evidence for interaction with circumstellar or circumbinary material. These nondetections strongly favor the double-degenerate scenario, but ultimately we are not able to prefer one progenitor scenario over the other given the existing models.

SN 2021aefx joins the growing sample of SNe Ia with unexpected photometric evolution during the first few days after explosion and highlights the importance of early discovery and classification and high-cadence multiwavelength follow-up in confronting existing models. Importantly, these types of light curves will not be available from the upcoming Legacy Survey of Space and Time at Vera C. Rubin Observatory with its nominal observing strategy (Ivezić et al. 2019). Specialized high-cadence surveys like DLT40, as well as robotic follow-up with facilities like Las Cumbres Observatory, will continue to be required to make progress in understanding SN Ia progenitors and explosions.

---

[19] However, Shen et al. (2021) can reproduce these observables with a 1.1 $M_\odot$ WD.

[20] However, Dessart et al. (2014) do expect unburned carbon in their "pulsational-delayed-detonation" models.

ORCID iDs

Griffin Hosseinzadeh ● https://orcid.org/0000-0002-0832-2974
David J. Sand ● https://orcid.org/0000-0003-4102-380X
Peter Lundqvist ● https://orcid.org/0000-0002-3664-8082
Jennifer E. Andrews ● https://orcid.org/0000-0003-0123-0062
K. Azalee Bostroem ● https://orcid.org/0000-0002-4924-444X
Yize Dong (董一泽) ● https://orcid.org/0000-0002-7937-6371
Daryl Janzen ● https://orcid.org/0000-0003-0549-3281
Jacob E. Jencson ● https://orcid.org/0000-0001-5754-4007
Michael Lundquist ● https://orcid.org/0000-0001-9589-3793
Nicolas E. Meza Retamal ● https://orcid.org/0000-0002-7015-3446
Jeniveve Pearson ● https://orcid.org/0000-0002-0744-0047
Stefano Valenti ● https://orcid.org/0000-0001-8818-0795
Samuel Wyatt ● https://orcid.org/0000-0003-2732-4956
Jamison Burke ● https://orcid.org/0000-0003-0035-6659
D. Andrew Howell ● https://orcid.org/0000-0003-4253-656X
Curtis McCully ● https://orcid.org/0000-0001-5807-7893
Estefania Padilla Gonzalez ● https://orcid.org/0000-0003-0209-9246
Craig Pellegrino ● https://orcid.org/0000-0002-7472-1279

Giacomo Terreran ● https://orcid.org/0000-0003-0794-5982
Lindsey A. Kwok ● https://orcid.org/0000-0003-3108-1328
Saurabh W. Jha ● https://orcid.org/0000-0001-8738-6011
Jay Strader ● https://orcid.org/0000-0002-1468-9668
Esha Kundu ● https://orcid.org/0000-0002-4807-379X
Stuart D. Ryder ● https://orcid.org/0000-0003-4501-8100
Joshua Haislip ● https://orcid.org/0000-0002-6703-805X
Vladimir Kouprianov ● https://orcid.org/0000-0003-3642-5484
Daniel E. Reichart ● https://orcid.org/0000-0002-5060-3673

References

Allison, J. R., Sadler, E. M., & Meekin, A. M. 2014, MNRAS, 440, 696
Ashall, C., Lu, J., Shappee, B. J., et al. 2022, ApJL, 932, L2
Astropy Collaboration, Price-Whelan, A. M., Sipőcz, B. M., et al. 2018, AJ, 156, 123
Badenes, C., Hughes, J. P., Bravo, E., & Langer, N. 2007, ApJ, 662, 472
Barbary, K., Bailey, S., Barentsen, G., et al. 2022, SNCosmo, Zenodo, doi:10.5281/zenodo.6363879
Benz, W., Hills, J. G., & Thielemann, F. K. 1989, ApJ, 342, 986
Björnsson, C.-I., & Lundqvist, P. 2014, ApJ, 787, 143
Blondin, S., Dessart, L., Hillier, D. J., & Khokhlov, A. M. 2013, MNRAS, 429, 2127
Blondin, S., & Tonry, J. L. 2007, ApJ, 666, 1024
Bloom, J. S., Kasen, D., Shen, K. J., et al. 2012, ApJL, 744, L17
Boehner, P., Plewa, T., & Langer, N. 2017, MNRAS, 465, 2060
Bostroem, K. A., Jha, S. W., Randriamampandry, S., et al. 2021, TNSCR, 3888, 1
Botyánszki, J., Kasen, D., & Plewa, T. 2018, ApJL, 852, L6
Branch, D., Dang, L. C., Hall, N., et al. 2006, PASP, 118, 560
Breeveld, A. A., Landsman, W., Holland, S. T., et al. 2011, in AIP Conf. Proc. 1358, Gamma Ray Bursts (Melville, NY: AIP), 373
Brown, T. M., Baliber, N., Bianco, F. B., et al. 2013, PASP, 125, 1031
Buckley, D. A. H., Burgh, E. B., Cottrell, P. L., et al. 2006, Proc. SPIE, 6269, 0A
Burke, J., Howell, D. A., Sarbadhicary, S. K., et al. 2021, ApJ, 919, 142
Buzzoni, B., Delabre, B., Dekker, H., et al. 1984, Msngr, 38, 9
Cao, Y., Kulkarni, S. R., Gal-Yam, A., et al. 2016, ApJ, 832, 86
Cao, Y., Kulkarni, S. R., Howell, D. A., et al. 2015, Natur, 521, 328
Chevalier, R. A., & Fransson, C. 2006, ApJ, 651, 381
Chomiuk, L., Soderberg, A. M., Chevalier, R. A., et al. 2016, ApJ, 821, 119
Clemens, J. C., Crain, J. A., & Anderson, R. 2004, Proc. SPIE, 5492, 331
Conley, A., Sullivan, M., Hsiao, E. Y., et al. 2008, ApJ, 681, 482
Crawford, S. M., Still, M., Schellart, P., et al. 2010, Proc. SPIE, 7737, 25
de Vaucouleurs, G., de Vaucouleurs, A., Corwin, H. G., et al. 1995, yCat, 7155, 0
Deckers, M., Maguire, K., Magee, M. R., et al. 2022, MNRAS, 512, 1317
Dessart, L., Blondin, S., Hillier, D. J., & Khokhlov, A. 2014, MNRAS, 441, 532
Dessart, L., Leonard, D. C., & Prieto, J. L. 2020, A&A, 638, A80
Di Stefano, R., Voss, R., & Claeys, J. S. W. 2011, ApJL, 738, L1
Dilday, B., Howell, D. A., Cenko, S. B., et al. 2012, Sci, 337, 942
Dimitriadis, G., Foley, R. J., Rest, A., et al. 2019, ApJL, 870, L1
Dimitriadis, G., Rojas-Bravo, C., Kilpatrick, C. D., et al. 2019, ApJL, 870, L14
Dubay, L. O., Tucker, M. A., Do, A., Shappee, B. J., & Anand, G. S. 2022, ApJ, 926, 98
Eggleton, P. P. 1983, ApJ, 268, 368
Elias-Rosa, N., Chen, P., Benetti, S., et al. 2021, A&A, 652, A115
Fink, M., Röpke, F. K., Hillebrandt, W., et al. 2010, A&A, 514, A53
Fitzpatrick, E. L. 1999, PASP, 111, 63
Folatelli, G., Phillips, M. M., Morrell, N., et al. 2012, ApJ, 745, 74
Foreman-Mackey, D. 2016, JOSS, 1, 24
Foreman-Mackey, D., Hogg, D. W., Lang, D., & Goodman, J. 2013, PASP, 125, 306
Gehrels, N., Chincarini, G., Giommi, P., et al. 2004, ApJ, 611, 1005
Guy, J., Astier, P., Baumont, S., et al. 2007, A&A, 466, 11
Harutyunyan, A. H., Pfahler, P., Pastorello, A., et al. 2008, A&A, 488, 383
Hoeflich, P. 2017, in Handbook of Supernovae, ed. A. W. Alsabti & P. Murdin (Cham: Springer)
Höflich, P., & Stein, J. 2002, ApJ, 568, 779
Hosseinzadeh, G., & Gomez, S. 2020, Light Curve Fitting, Zenodo, doi:10.5281/zenodo.4312178
Hosseinzadeh, G., Sand, D. J., Valenti, S., et al. 2017, ApJL, 845, L11

Howell, D. A. 2011, NatCo, 2, 350
Howell, D. A., Sullivan, M., Perrett, K., et al. 2005, ApJ, 634, 1190
Hunter, J. D. 2007, CSE, 9, 90
Iben, I., & Tutukov, A. V. 1984, ApJS, 54, 335
Ivezić, Ž., Kahn, S. M., Tyson, J. A., et al. 2019, ApJ, 873, 111
Jha, S., Riess, A. G., & Kirshner, R. P. 2007, ApJ, 659, 122
Jha, S. W., Maguire, K., & Sullivan, M. 2019, NatAs, 3, 706
Jiang, J.-a., Doi, M., Maeda, K., et al. 2017, Natur, 550, 80
Jiang, J.-a., Maeda, K., Kawabata, M., et al. 2021, ApJL, 923, L8
Justham, S. 2011, ApJL, 730, L34
Kasen, D. 2010, ApJ, 708, 1025
Kasen, D., Röpke, F. K., & Woosley, S. E. 2009, Natur, 460, 869
Katz, B., & Dong, S. 2012, arXiv:1211.4584
Khokhlov, A. M. 1991, A&A, 245, 114
Kniazev, A. Y., Gvaramadze, V. V., & Berdnikov, L. N. 2016, MNRAS, 459, 3068
Kniazev, A. Y., Gvaramadze, V. V., & Berdnikov, L. N. 2017, in Stars: From Collapse to Collapse, Proc. of a conf., 510, ed. Y. Y. Balega et al. (San Francisco, CA: ASP), 480
Kollmeier, J. A., Chen, P., Dong, S., et al. 2019, MNRAS, 486, 3041
Kundu, E., Lundqvist, P., Pérez-Torres, M. A., Herrero-Illana, R., & Alberdi, A. 2017, ApJ, 842, 17
Kundu, E., Lundqvist, P., Ryder, S. D., et al. 2021, ATel, 15077, 1
Kushnir, D., Katz, B., Dong, S., Livne, E., & Fernández, R. 2013, ApJL, 778, L37
Li, W., Bloom, J. S., Podsiadlowski, P., et al. 2011, Natur, 480, 348
Li, W., Wang, X., Vinkó, J., et al. 2019, ApJ, 870, 12
Lira, P. 1996, Master's thesis, Universidad de Chile
Liu, Z. W., Pakmor, R., Röpke, F. K., et al. 2012, A&A, 548, A2
Liu, Z.-W., Pakmor, R., Seitenzahl, I. R., et al. 2013, ApJ, 774, 37
Livne, E. 1990, ApJL, 354, L53
Lorén-Aguilar, P., Isern, J., & García-Berro, E. 2009, A&A, 500, 1193
Lundqvist, P., Mattila, S., Sollerman, J., et al. 2013, MNRAS, 435, 329
Lundqvist, P., Nyholm, A., Taddia, F., et al. 2015, A&A, 577, A39
Lundqvist, P., Kundu, E., Pérez-Torres, M. A., et al. 2020, ApJ, 890, 159
Magee, M. R., & Maguire, K. 2020, A&A, 642, A189
Magee, M. R., Maguire, K., Kotak, R., et al. 2020, A&A, 634, A37
Magee, M. R., Sim, S. A., Kotak, R., & Kerzendorf, W. E. 2018, A&A, 614, A115
Maguire, K. 2017, in Handbook of Supernovae, ed. A. W. Alsabti & P. Murdin (Berlin: Springer)
Maguire, K., Taubenberger, S., Sullivan, M., & Mazzali, P. A. 2016, MNRAS, 457, 3254
Maoz, D., Mannucci, F., & Nelemans, G. 2014, ARA&A, 52, 107
Marietta, E., Burrows, A., & Fryxell, B. 2000, ApJS, 128, 615
Marion, G. H., Brown, P. J., Vinkó, J., et al. 2016, ApJ, 820, 92
McCully, C., Turner, M., Volgenau, N., et al. 2018, LCOGT/Banzai: Initial Release, Zenodo, doi:10.5281/zenodo.1257560
McMullin, J. P., Waters, B., Schiebel, D., Young, W., & Golap, K. 2007, ASPC, 376, 127
Miller, A. A., Cao, Y., Piro, A. L., et al. 2018, ApJ, 852, 100
Miller, A. A., Magee, M. R., Polin, A., et al. 2020, ApJ, 898, 56
NASA HEASARC 2014, HEAsoft: Unified Release of FTOOLS and XANADU, Astrophysics Source Code Library, ascl:1408.004
Ni, Y. Q., Moon, D.-S., Drout, M. R., et al. 2022, NatAs, 6, 568
Nomoto, K. 1982, ApJ, 257, 780
Nomoto, K., Thielemann, F. K., & Yokoi, K. 1984, ApJ, 286, 644
Nugent, P. E., Sullivan, M., Cenko, S. B., et al. 2011, Natur, 480, 344
Oliphant, T. E. 2006, A Guide to NumPy (USA: Trelgol Publishing)
Onori, F., Carini, R., D'Avanzo, P., Melandri, A., & Bruch, R. J. 2021, TNSCR, 3899, 1
Pakmor, R., Kromer, M., Taubenberger, S., et al. 2012, ApJL, 747, L10
Pan, K.-C., Ricker, P. M., & Taam, R. E. 2010, ApJ, 715, 78

Pan, K.-C., Ricker, P. M., & Taam, R. E. 2012, ApJ, 750, 151
Parrent, J. T., Thomas, R. C., Fesen, R. A., et al. 2011, ApJ, 732, 30
Perlmutter, S., Aldering, G., Goldhaber, G., et al. 1999, ApJ, 517, 565
Phillips, M. M. 1993, ApJL, 413, L105
Phillips, M. M., Lira, P., Suntzeff, N. B., et al. 1999, AJ, 118, 1766
Piro, A. L., & Morozova, V. S. 2016, ApJ, 826, 96
Polin, A., Nugent, P., & Kasen, D. 2019, ApJ, 873, 84
Polin, A., Nugent, P., & Kasen, D. 2021, ApJ, 906, 65
Poznanski, D., Prochaska, J. X., & Bloom, J. S. 2012, MNRAS, 426, 1465
Prieto, J. L., Chen, P., Dong, S., et al. 2020, ApJ, 889, 100
Reynolds, S. P., Williams, B. J., Borkowski, K. J., & Long, K. S. 2021, ApJ, 917, 55
Riess, A. G., Filippenko, A. V., Challis, P., et al. 1998, AJ, 116, 1009
Roming, P. W. A., Kennedy, T. E., Mason, K. O., et al. 2005, SSRv, 120, 95
Röpke, F. K., Woosley, S. E., & Hillebrandt, W. 2007, ApJ, 660, 1344
Röpke, F. K., Kromer, M., Seitenzahl, I. R., et al. 2012, ApJL, 750, L19
Rubin, V. C., Westpfahl, D., & Tuve, M. 1974, AJ, 79, 1406
Sabbi, E., Calzetti, D., Ubeda, L., et al. 2018, ApJS, 235, 23
Sand, D. J., Graham, M. L., Botyánszki, J., et al. 2018, ApJ, 863, 24
Sand, D. J., Amaro, R. C., Moe, M., et al. 2019, ApJL, 877, L4
Sand, D. J., Sarbadhicary, S. K., Pellegrino, C., et al. 2021, ApJ, 922, 21
Sault, R. J., Teuben, P. J., & Wright, M. C. H. 1995, in ASP Conf. Ser. 77, Astronomical Data Analysis Software and Systems IV (San Francisco, CA: ASP), 433
Savitzky, A., & Golay, M. J. E. 1964, AnaCh, 36, 1627
Schlafly, E. F., & Finkbeiner, D. P. 2011, ApJ, 737, 103
Schlafly, E. F., Finkbeiner, D. P., Schlegel, D. J., et al. 2010, ApJ, 725, 1175
Science Software Branch at STScI 2012, PyRAF: Python Alternative for IRAF, Astrophysics Source Code Library, ascl:1207.011
SDSS Collaboration, Albareti, F. D., Allende Prieto, C., et al. 2017, ApJS, 233, 25
Seaquist, E. R., Krogulec, M., & Taylor, A. R. 1993, ApJ, 410, 260
Seitenzahl, I. R., Ciaraldi-Schoolmann, F., Röpke, F. K., et al. 2013, MNRAS, 429, 1156
Shappee, B. J., Piro, A. L., Stanek, K. Z., et al. 2018, ApJ, 855, 6
Shappee, B. J., Holoien, T. W.-S., Drout, M. R., et al. 2019, ApJ, 870, 13
Shen, K. J., & Bildsten, L. 2014, ApJ, 785, 61
Shen, K. J., Boos, S. J., Townsley, D. M., & Kasen, D. 2021, ApJ, 922, 68
Siebert, M. R., Dimitriadis, G., Polin, A., & Foley, R. J. 2020, ApJL, 900, L27
Silverman, J. M., & Filippenko, A. V. 2012, MNRAS, 425, 1917
Stetson, P. B. 2000, PASP, 112, 925
Tartaglia, L., Sand, D. J., Valenti, S., et al. 2018, ApJ, 853, 62
Torres, S., Briceño, C., & Quint, B. 2017, Goodman HTS Pipeline Documentation 1.3.6, https://soardocs.readthedocs.io/projects/goodman-pipeline/
Tucker, M. A., Shappee, B. J., & Wisniewski, J. P. 2019, ApJL, 872, L22
Tucker, M. A., Shappee, B. J., Vallely, P. J., et al. 2020, MNRAS, 493, 1044
Tucker, M. A., Ashall, C., Shappee, B. J., et al. 2021, ApJ, 914, 50
Tully, R. B., & Fisher, J. R. 1977, A&A, 54, 661
Valenti, S., Sand, D., Pastorello, A., et al. 2014, MNRAS, 438, L101
Valenti, S., Howell, D. A., Stritzinger, M. D., et al. 2016, MNRAS, 459, 3939
Valenti, S., Sand, D. J., Wyatt, S., et al. 2021, TNSTR, 3864, 1
Vallely, P. J., Fausnaugh, M., Jha, S. W., et al. 2019, MNRAS, 487, 2372
Wang, X., Wang, L., Filippenko, A. V., Zhang, T., & Zhao, X. 2013, Sci, 340, 170
Webbink, R. F. 1984, ApJ, 277, 355
Wells, D. C. 1985, in Data Analysis in Astronomy, Proc. of the 1st Workshop, ed. V. di Gesu et al. (New York: Plenum Press), 195
Whelan, J., & Iben, I. 1973, ApJ, 186, 1007
Woosley, S. E., & Kasen, D. 2011, ApJ, 734, 38
Wyatt, S. D., Sand, D. J., Hsiao, E. Y., et al. 2021, ApJ, 914, 57
Zhang, K., Wang, X., Zhang, J., et al. 2016, ApJ, 820, 67